ADVANCED MATERIALS INTERFACES
www.advmatinterfaces.de

Size-Controlled Nanosculpture of Cylindrical Pores across Multilayer Graphene via Photocatalytic Perforation

Albert Guirguis, Ludovic F. Dumée, Daniel J. Eyckens, Melissa K. Stanfield, Yanting Yin, Gunther G. Andersson, Lingxue Kong, and Luke C. Henderson**

One of the bottlenecks in realizing the potential of nanoporous graphene assemblies is the difficulty of engineering narrow pores and high surface density distributions, with a nanometer resolution across multilayer graphene assemblies using scalable approaches. Here, the authors develop a photocatalyzed perforation protocol to incorporate nanopores across modified graphene assemblies via localizing the oxidation during the photo-excitation process between photo-initiators and graphitic assemblies under the ultraviolet–visible stimuli. Nanopores are engineered across the graphene nanostructures with a pore size range varying from 20 to 100 nm depending on the irradiation duration, as well as tunable densities of 10^1–10^3 pores/μm^2 on the same order of the loaded nanocatalysts to the graphene surfaces. By fine-tuning the graphene chemistry and the physical dimension of photo-initiators, as well as their concentrations across graphitic planes used during the perforation, the diameter, and the density distributions of generated nanopores across graphene, can be rationally confined, avoiding merging between pores during the nanopore formation. These porosity parameters engineered across graphene nanosieves are in the same order obtained by other nanolithographic techniques. Plus, this sustainable route may boost the potential of porous graphene assemblies in energy-efficient nanotechnologies based on separation and catalytic processes.

1. Introduction

Nanoporous graphene (NPG) materials are a mesh architecture with size-controlled pores ranging from sub-nanometer[1–3] to a few nanometers and tunable surface densities across the 2D graphene nanostructure.[4] The microstructure morphology and physicochemical properties of NPG materials have been exploited in sieving, sensing, energy harvesting, and catalysis applications.[5–8]

The morphological properties of NPG materials in terms of sizes, densities distributions, and depths, as well as geometrical shapes ranging across single-, or few-layer graphene sheets, have solely relied on the applied perforation methodologies.[4] The state-of-art of perforation technology for 2D nanoporous nanostructures can be classified into either stochastic/guided-etching or guided-growth techniques based on the achieved pore-size and surface-pore distribution ranges.[4,9] Cylindrical pores with narrow size distribution and high-density surface distributions are still desired for engineering porous graphene-derived nanoassemblies. The capability to induce such architectural features across graphene will therefore enhance their potential in a variety of nanotechnologies based on separation and catalytic processes.[9]

One promising perforation methodology is photocatalytic perforation, a particulate-assisted etching protocol. The proof of concept was demonstrated via arranging nanocatalysts over graphene surfaces to accelerate the oxidation upon the photo-irradiation process with ultraviolet (UV)–visible stimuli. Consequently, the achieved

A. Guirguis, L. F. Dumée, M. K. Stanfield, L. Kong, L. C. Henderson
Institute for Frontier Materials
Deakin University, Geelong
Waurn Ponds, Victoria 3216, Australia
E-mail: aguirguis@deakin.edu.au; luke.henderson@deakin.edu.au
L. F. Dumée
Department of Chemical Engineering
Khalifa University
SAN Campus, Abu Dhabi, UAE
The ORCID identification number(s) for the author(s) of this article can be found under https://doi.org/10.1002/admi.202102129.

DOI: 10.1002/admi.202102129

D. J. Eyckens
Commonwealth Scientific and Industrial Research Organization (CSIRO)
Manufacturing, Clayton, Victoria 3168, Australia
Y. Yin, G. G. Andersson
Flinders Institute for Nanoscale Science and Technology
Flinders University
Adelaide, SA 5042, Australia
Y. Yin, G. G. Andersson
Flinders Microscopy and Microanalysis
College of Science and Engineering
Flinders University
Adelaide, SA 5042, Australia

porosity parameters across NPG nanostructure have mostly followed the morphological properties of initially designed particulate-template, used to confine energetic radicals generated during the photo-excitation mechanism.[10,11] This leads to etching carbon clusters across graphitic planes in contact with the loaded nanocatalysts. However, the nanopatterning of these nanocatalysts to form a precise particulate template, as well as the reduction of the kinetics of nanoclusters across graphene surfaces during the loading process, has not yet been addressed. This is to avoid the possible generation of nano- and micro-cracks around the nonintentional clusters of nanocatalysts, which could be probably formed upon the irradiation process. The correlation between the kinetic mechanism and the variation of pore formation across the graphene structure, concerning expanding and shrinking, as well as the evolution of pore-depth across a few nanometers in thickness, have not yet been evaluated across graphene assemblies during the UV–visible irradiation process.[11–13]

The surface chemistry, as well as the interlayer Van der Waals attractions between sheets, can be exploited to assemble such sheets into sub-nanometer,[14] or few-nanometer[15] assemblies in thickness via a variety of deposition techniques.[16] Such assembled films with high adsorption capacities,[17,18] can be used as raw materials to anchor the colloidal nanocatalysts and array them across their graphitic nanostructures during the loading process. These 2D nano-assemblies are however suffered from spatially varying surface chemistry[19] due to the merging between sheets and are highly expected to accelerate the kinetics of the nanoclustering of nanocatalysts near these regions, especially nanowrinkles.[20] Consequently, this nanocoalescence of the catalysts in these graphitic groves will drastically cause the merging of the pores, causing microcracks upon the activation during the perforation process. Engineering the surface of these graphene assemblies with uniform chemistry is, therefore, a prerequisite to synthesizing NPG without the need for external nanotemplates.

In this research, we demonstrate that a narrow pore size distribution and high surface density distribution can be engineered through grafted graphene oxide (GO) assemblies, utilizing catalytic-etching of arrayed nanocatalysts across their graphitic basal planes. The effect of the surface chemistry of graphene in designing particulate-nanotemplates with different sizes and surface densities was evaluated. The porosity parameters achieved across perforated nanostructures were further investigated and then correlated to the perforation conditions including colloidal concentrations of nanocatalysts applied, or UV–visible irradiation durations during the etching process. Conical and cylindrical nanochannels were perforated with depths ranging from sub-nanometer to a few nanometers, which were well-matched with the thickness of these graphitic assemblies based on pristine and grafted graphene chemistries, respectively. The pore formation across graphene prior to and post the irradiation was systemically investigated in the light of the defect engineering analysis. The proposed work demonstrated a photocatalytic perforation protocol, as an effective methodology for tailoring cylindrical nanopores across multilayer graphene assemblies that can be utilized as custom-designed nanosieves for a variety of separation and catalytic applications.

2. Experimental Section

2.1. Electrochemical Grafting of Graphene Assemblies via Aryl-Diazonium Chemistry

Aqueous GO colloidal (0.1 wt%, Graphenano Company, Spain) was purified via centrifuge (Allegra X-12R Centrifuge) at 3000 revolutions per minute (RPM) for 10 min to narrow down the size of 2D sheets, as well as remove such nonexfoliated graphite particles.[14] Multilayer GO assemblies were prepared via spin-coating of the centrifuged GO colloidal on SiO_x/Si substrates, which were previously were treated in Piranha solution (70:30 v/v concentrated H_2SO_4 and 30% H_2O_2) for 60 min prior to the deposition process. These assemblies were obtained via casting with a fixed volume (10 µL) of GO colloidal at the substrate and then spinning at 500, 800, 1600, and 2000 RPM for 30 s per each speed.

These suspended GO assemblies over SiO_x/Si supports were grafted electrochemically with 4-carboxybenzenediazonium tetrafluoroborate diazonium ($C_7H_5BF_4N_2O_2$) salts and the detailed synthesis and characterization are discussed in the Section S1, Supporting Information. The electrochemical grafting was carried out using Metrohm Autolab potentiostat from (Kanaalweg, The Netherlands) inside a homemade cell, as adapted from the authors' previous methods.[21–25] The suspended GO sample was mounted typically to serve as a working electrode, Pt-wire and Ag/AgCl was used as the counter and reference electrodes, respectively. The sample was immersed in a solution of 1 mM diazonium salt and a 1 M supporting electrolyte solution of tetrabutylammonium hexafluorophosphate ($TBAPF_6$) in acetonitrile.[26] The grafting process was conducted through ramping voltage between +1.0 and −1.0V versus Ag/AgCl at a rate of 0.02 V s^{-1} over three cycles. Data was acquired by NOVA software from (Kanaalweg, The Netherlands). All grafted samples were rinsed in deionized (DI) water, and ethanol sequentially, to remove the excess molecules adsorbed across grafted graphene assemblies. For the evaluation of the electrochemical grafting, the grafting experiments were also carried in the presence of a Buckypaper from reduced-graphene oxide (RGO), as a reference sample of low-oxygen content graphitic nanostructures, which was treated via hydrazine (N_2H_2) vapor exposure.[27]

2.2. Nanopatterning of Pristine and Grafted Graphene Oxide Assemblies with Zinc Oxide Nanocatalysts

The capability of the grafted functional groups across graphitic planes of the GO nanostructure to adsorb and arrange suspended zinc oxide (ZnO) nanocatalysts into a stable colloidal was assessed based on pristine and diazonium chemistry. This was performed via vertically dipping the assembled nanostructures over SiO_x/Si supports into a stable ZnO colloidal (Sigma-Aldrich, average particle size, typically of 20 ± 15 nm) at ambient conditions without any stimulus. The nanopatterning of such ZnO nanocatalysts across those loaded samples based on pristine and grafted GO chemistries was engineered by using different concentrations of ZnO colloidal during the loading process that includes 10, 50, and 100 ppm prior to extraction at a fixed dipping duration, typically 5 min, separately. The extraction

process was performed via sonicating suspensions (QSONICA 700) for 10 min with a pause of 5 s and then centrifuged for 10 min at 8000 rpm (Beckman and Coulter Allegra X-12R). The nanocatalysts were extracted from the resulted surfactant of the previously centrifuged samples to avoid any nanoclusters, suspended in the colloidal prior to use in the loading process. To ensure the stability of such anchored ZnO nanocatalysts across those loaded samples, all samples were washed with an excess of pure ethanol and then DI water for several cycles, consecutively.

The kinetic of ZnO clustering across the samples during the loading process was investigated with another ZnO colloidal, prepared via the sol–gel assisted by ultrasonic irradiation technique,[28] as discussed in Section S2, Supporting Information. A relatively high concentration of as-prepared ZnO colloidal was used during these experiments, typically of 200 ppm to be loaded to the GO samples over different durations that include 5, 30, and 60 min, separately. The size and density distributions of ZnO nanocatalysts across graphitic planes of those loaded samples were investigated via scanning electron microscope (SEM) and atomic force microscope (AFM) analyses over relatively large scans for evaluating the nanoclustering, as well as ensuring the homogeneity of such loaded samples. Furthermore, the atomic concentration, as well as chemistry of loaded ZnO nanocatalysts to pristine and grafted GO surfaces were further investigated via X-ray photoelectron spectroscopy (XPS) and then correlated to the loading conditions.

2.3. Ultraviolet and Visible Etching Irradiation

The loaded GO samples with ZnO nanocatalysts, as pore-mediators were irradiated via UV–visible radiations (OmniCure S2000 UV Lamp). Pristine- and grafted-GO via diazonium salt samples were illuminated by UV light source with a measured irradiance of 1100 mW cm^{-2} and a light filter of wavelength between 320 and 480 nm.[29,30] All samples were covered with a water-slap with a fixed volume (10 µL) per a 1-cm^2 surface area to provide interaction between these loaded nanocatalysts and the graphitic planes during the etching process. The range of UV wavelength was carefully selected to be not less than 320 nm for providing the threshold activation energy for ZnO semiconducting materials and at the same time minimizing the generation of other oxygenous radicals, such as ozone (O_3), which was likely, to be generated at lower wavelength ranges of the UV spectrum.[13,31] The development of the relative penetration depth of the loaded nanocatalysts over the multilayer GO assemblies was investigated via SEM and AFM analyses over different durations, including 60, 360, and 1080 min, separately, at a fixed irradiance (1100 mW cm^{-2}).

2.4. Removal of Nanocatalysts Post the Irradiation Process

The removal of the intercalated ZnO nanocatalysts across multilayer graphene samples was performed via treating the irradiated samples in the acidic medium.[32] The dissolution kinetics of such nanocatalysts during the acid treatment in 1 M hydrogen chloride (HCl) was systemically studied by investigating the morphology of the treated samples via SEM analysis and AFM mapping over different durations that include 1, 6, 15, 72 and 168 h. To evaluate the long-term chemical stability of pristine materials in this acidic medium, the GO samples were treated in 1 M HCl over short duration periods between 3 and 24 h, as well as longer duration periods ranging from 48 to 168 h, separately at ambient conditions. The variation of surface chemistry and crystallographic properties as the function of atomic defects across those treated GO samples were investigated via ATR-FTIR and Raman spectroscopy, as well as AFM mapping, and then compared to the as-prepared samples.

2.5. Characterization Techniques

2.5.1. Microstructure Analysis

SEM (Zeiss Supra 55VP FEG) was used to investigate the microstructure of graphene samples prior to and post the perforation process at a 2 kV of acceleration voltage and a working distance of 5 mm with 30 µm-aperture. The suspended multilayer graphene assemblies on SiO_x (280 nm)/Si supports were electrically grounded on aluminum holders with carbon tape without any coating. AFM (MultiMode 8-HR, Bruker) was further used to investigate any variation of the morphological properties of 2D perforated graphene samples. AFM mapping was conducted in ScanAssist mode via a silicon nitride probe (SCANASYST-AIR, Bruker) with a radius of 2–12 nm and a force constant of 0.4 N m^{-1}. The pore profiles of sizes, densities distributions, and depths, as well as geometrical shapes ranges across perforated samples, were estimated through processing either AFM maps with NanoScope Analysis 2.0 software or SEM micrographs with the ImageJ software over three different locations at the nanometer scale.

2.5.2. The Variation of Crystallographic Properties of Graphene Samples during the Pore Formation via Raman Analysis

The pore formation across graphene samples prior to and post the UV irradiation was systemically investigated via Raman spectroscopy. Their intrinsic crystallinity and defect density were assessed by micro-Raman spectroscopy technique (Renishaw inVia) with an excitation laser of 514 nm and a 100× objective lens to achieve a very fine beam spatial resolution, nearly 300 nm. A grating filter with 2400 grooves/mm was employed for the monochromatization of the signals. The power was kept to 10% of the total power (1.2 mW without the objective lens) to prevent damage to the graphitic planes.[29] The integral time for a single acquisition was fixed at 10 s for all measurements. All Raman spectra were collected in the wavenumber range between 1000 and 3200 cm^{-1} and interpreted with Wire 3.2 software. The Raman spectra were evaluated over five points over each sample and then averaged to maintain the statistical aspect of reported values.

2.5.3. Surface Chemistry Analysis

The evaluation of the zinc interstitial and oxygen atomic concentrations across the loaded graphene samples with ZnO

nanocatalysts based on pristine and grafted GO surfaces were further investigated via XPS analysis. Data were collected with a photoelectron spectrometer (Phoibos 100, SPECS, Berlin) while a nonmonochromatized Mg Kα X-ray source was applied for X-ray emission with an excitation energy of 1253.6 eV at 200 W and 12K eV. The analysis chamber had a base pressure of a few 10^{-10} mbar. All surveys and high-resolution spectra were measured at 40 and 10 eV pass energies with 1 and 20–25 scans, respectively. A selected area using Ø-3 mm aperture was analyzed using low-magnification mode on each sample over five different spots for statistical relevance. The spot area on a sample was a circle of Ø-1.5 mm. Peak analyses were performed with the CasaXPS software, using a weighted sum of Gaussian and Lorentzian component curves GL (p), where (p) parameter was equal to 30. The measured spectra were further calibrated with Zn 2p3/2 at 1021.8 eV of ZnO due to a lack of C—C for reference of the samples.[33] With this calibration condition, C sp^2 could be found at 284.2 ± 0.2 eV while graphitic oxide could be identified at 286.3 ± 0.2 eV. The fitting of C resulted in a further presence of C—O species at 285.6 ± 0.2 eV which could be assigned to partially oxidized graphitic C which was not bound to the carboxyl group ($C_6H_x(COOH)_{6-x}$).[34] The as-prepared and grafted GO samples were calibrated with C sp^2 found in ZnO doped samples for a consistent observation.

2.5.4. Characterizations of Zinc Oxide Nanocatalytic Colloidal

ZnO colloid was prepared via sol–gel assisted by ultrasonic irradiation technique, as adopted in the literature[28] and discussed in Section S2, Supporting Information. The concentration of the previously prepared ZnO colloidal was estimated via UV–visible spectroscopy analysis based on a commercial colloidal, as provided by the manufacturer (Sigma Aldrich) stand on the calibration curve (Figure S5, Supporting Information). The hydrodynamic diameter of suspended ZnO nanoparticles in ethanol colloidal was assessed prior to utilizing them in the nanopatterning process via dynamic light scattering (MALVERN Zetasizer Nano, ATA scientific instruments), with a reflective index, n of 1.4 and absorption coefficient of 0.1 for ZnO materials over three measurements, consecutively in ambient conditions without any sonication. All samples were left to stabilize for 120 s prior to collecting their measurements. Each sample was characterized by three different preparations per condition for confirming the revealed trends. The size distributions of those prepared nanocatalysts were intensively characterized via DLS analysis and AFM mapping.

3. Results and Discussions

To perforate graphene with a narrow, downsize distribution of nanopores across 2D nano-assemblies, a particulate-assisted etching methodology was proposed. This is performed in a four-step process of UV–visible irradiation of ZnO nanocatalysts on surface-modified graphene, followed by the removal of nanocatalysts via acid treatment (**Figure 1**).

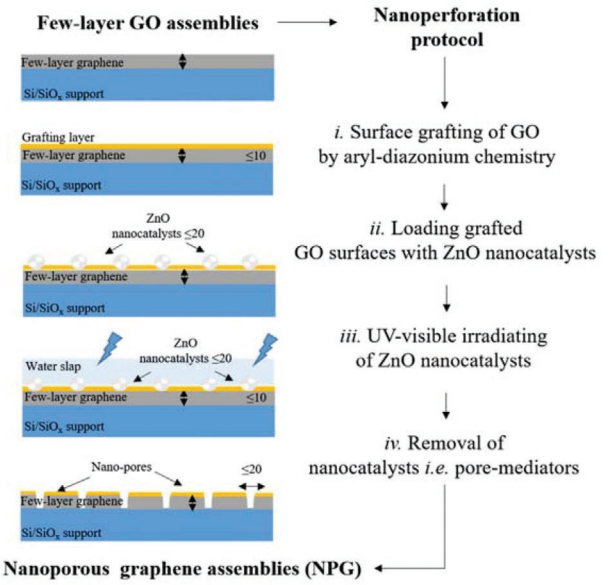

Figure 1. Schematic diagram illustrating four-step photocatalytic perforation methodology to engineer nanopores across few-layer GO assemblies: i) Surface grafting via diazonium salt, ii) loading the surface of grafted GO nanostructures by ZnO nanocatalysts, iii) irradiation of previously loaded samples with ZnO nanocatalysts via UV–visible stimuli, and iv) removal of the nanocatalysts from the perforated samples via acid treatment.

3.1. Electrochemical Grafting of Graphene via Aryl-Diazonium Chemistry

First, the GO sheets were assembled over SiO_x/Si substrates via spin-coating and their topological characteristics were investigated via AFM, as illustrated in **Figure 2**A. The assembled GO layer structure based on 2D sheets exhibited a maximum thickness of ≤10 nm over a 5 µm scan size from three representative height profiles. These GO nano-assemblies also exhibited a few nanowrinkles, that is, graphitic nanoclusters due to the misalignments between cross-linked sheets during the assembly process, observed as bright spots (Figure S1, Supporting Information).

The prepared GO samples were grafted via direct electrochemical reduction of 4-carboxybenzenediazonium tetrafluoroborate in an aqueous electrolyte ($TBAPF_6$, 1.0 M) solution (cyclic voltammograms and controls in Supporting Information). This process introduces a covalently grafted layer of carboxyphenyl groups to the graphene surface and increases the density of carboxylic acid functional groups across the basal and edge planes of the assembled graphitic nanostructures. No significant changes, relative to control samples, were observed in the morphological properties across graphitic planes after surface grafting (Figure 2B). However, several bright nano-islands were observed on the graphene surface across those samples that were grafted using a 1 mM solution of the diazonium salt. This is likely to be observed across the graphitic planes after electrochemical grafting due to the lack of diffusional control of the diazonium radicals instantaneously generated in the solution and the graphitic surface during the salt reduction.[35,36] Otherwise, the surface of grafted samples appeared very uniform, achieving an RMS roughness ten times higher, compared

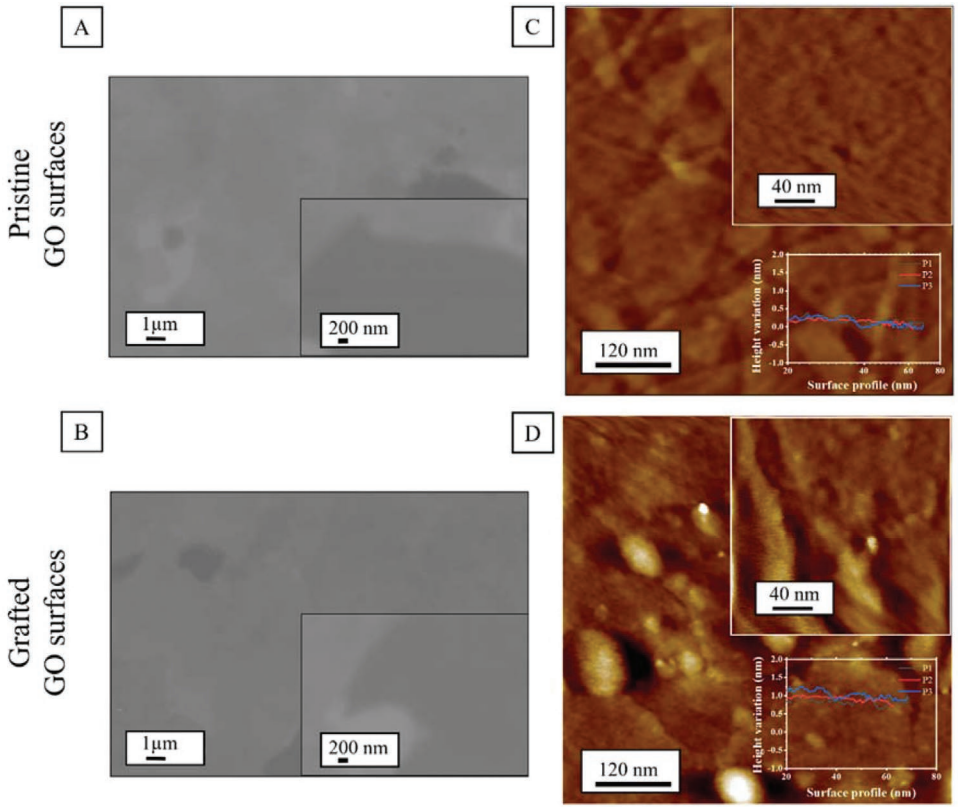

Figure 2. The morphology assessment of GO assembled on SiO_x/Si substrates prior to and post the electrochemical grafting process. A,B) FESEM micrographs and C,D) 2D-AFM maps for graphene oxide (GO) assemblies prior to and post the electrochemical grafting with 1 M 4-carboxybenzenediazonium tetrafluoroborate diazonium salt; inserts represent few representative surface roughness profiles across the pristine and grafted basal graphitic planes, respectively. Color bars for the heights correspond to 10 and 5 nm of a resolution map at 120 and 40 nm scale bar, respectively.

to the graphitic planes across the as-prepared samples, typically of 0.2 nm (check the height profiles inserted into Figure 2C,D). The inability of AFM to visualize the individual adsorbed species across the constructed grafting layer may be attributed to the packed arrangement of these grafted species into a uniform layer morphology,[35] which has been revealed from the height profiles across their maps.

In order to suppress the difficult-to-observe constructed grafting layer, typically ≤1 nm[37] across the grafted GO samples, control grafting experiments were conducted using chemically RGO Buckypaper. This serves as reference material of low-oxygen content graphitic nanostructures, under the same experimental grafting conditions. The surface chemistry and wettability properties of RGO samples (control and surface modified) were also investigated via measuring their ATR-FTIR spectra and correlating these to their water contact angle values. A significant decrease was observed in the intensity overall bands across the FTIR spectrum of GO samples post the N_2H_2 vapor exposure. This has led to poor wettability properties for such RGO samples, achieving a water contact angle value, typically 89 ± 2°, which is four times higher compared with untreated GO samples. This confirms that most of the oxygen-containing functional groups have almost vanished post the hydrazine vapor exposure.[38,39] On the other hand, the RGO samples, which were grafted via 1 mM diazonium exhibited a contact angle value of 74 ± 3°, which is nearly 15% less compared to as-produced RGO samples. This improvement in the wettability properties of those grafted RGO samples confirms the recovery of carboxylic groups across graphene samples post the grafting process, which agreed with the FTIR analysis, as illustrated in Figure S4D,E, Supporting Information. Therefore, these revealed trends suggest a successful construction of a grafting layer, which may be covalently attached to 2D sheets across the graphene assemblies.[36]

3.2. Nanopatterning of Zinc Oxide Nanocatalysts across Pristine and Grafted Graphene Structure

The nanopatterning of ZnO nanocatalysts, as a particulate-template with tunable densities and sizes across graphene nanostructures, is extremely crucial to generate nanoporous graphene structures of engineered pore densities, as well as narrow pore size distributions, post the photocatalytic perforation process.[4,9] To control particle density and its nucleated size across graphene surface, as well as reduce the kinetics of agglomeration during the loading process, the anchoring of such nanocatalysts was performed by vertically dipping. The pristine and grafted graphene samples were dipped into colloidal solutions with suspended ZnO particles (sized of 20 nm with a cut-off size of ≤100 nm, as was characterized in

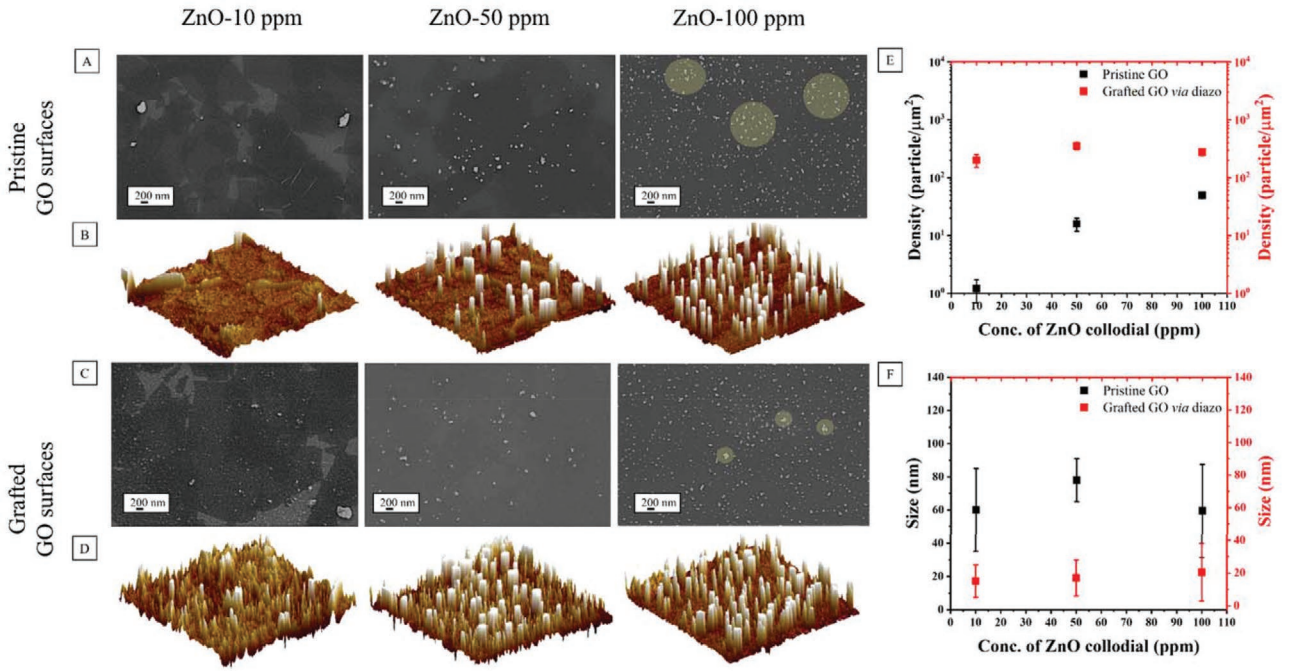

Figure 3. Morphological structures and surface chemistry analysis of the loaded graphene samples with ZnO nanocatalysts at different loading conditions. A,B) FESEM micrographs and C,D) 3D-AFM maps for the loaded graphene oxide (GO) samples at different amounts of nanocatalysts based on pristine and grafted chemistries (color bar for the height corresponds to 20 nm of a 1400 nm map size). E,F) The surface densities and sizes distributions of the nanocatalysts across the loaded samples based on AFM analysis.

Figure S6A,B, Supporting Information) at different concentrations including 10, 50, and 100 ppm at a fixed dipping duration (5 min) post the extraction process, separately.

Loaded samples based on pristine and grafted GO were investigated by SEM analysis and AFM mapping to estimate the density and sizes distributions of ZnO nanocatalysts and the results are summarized in Table S2, Supporting Information. Such morphological properties were typically correlated to the concentration of nanoparticles, remaining in the used supernatant solution post the extraction process. **Figures 3**A and 3C represent loaded ZnO nanoparticles across assembled layers across decorated samples based on pristine and diazonium grafted samples, respectively. The density of ZnO nanoparticles across pristine GO structure was found to linearly increase with respect to the concentration of ZnO colloidal used during the loading process at a fixed duration (5 min). In this regard, GO samples that were loaded with 10 ppm exhibited a low distribution of particles across their graphitic basal planes, typically 1.2 ± 0.5 particle/μm^2, while those loaded with 50 and 100 ppm exhibited density values of 16 ± 4 and 50 ± 5 particle/μm^2, respectively. Interestingly, other loaded samples based on the installed carboxyl moieties exhibited similar density values at the same range of loading conditions. It was also noticed that the probability of such nanocatalyst clustering across loaded samples based on pristine GO chemistry increased, compared with the other samples with surface-modified substrates, particularly at a high colloidal concentration (100 ppm), as highlighted by yellow spots in their micrographs.

Furthermore, the influence of the concentration of ZnO nanoparticles used on their size distributions across the loaded samples based on surface chemistry was evaluated via AFM analysis (Figure 3B,D). An increase in the size distribution of ZnO nanocatalysts regardless of the loading conditions was observed across those loaded samples based on the pristine materials, which confirms that a minimal agglomeration of those loaded ZnO nanocatalysts has occurred across loaded GO samples. However, the grafted GO samples showed narrow size distribution ranges in comparison with the pristine samples. For instance, the loaded samples with 50 ppm exhibited an average size distribution of anchored ZnO particles across grafted graphitic planes, typically of 17 ± 11 nm, as well as a surface density of 300 ± 50 particle/μm^2, which were not changed much in the loaded samples at 100 ppm, as exhibited in Figure 3E,F. These findings were found however to be inconsistent with those obtained via SEM analysis, which may be attributed only to the limitation of the scanning resolution. To further understand the development of nanoclustering occurred of such loaded ZnO nanocatalysts across the GO sheets during the loading process, control loading experiments were also conducted with a concentrated colloidal solution, as characterized, and discussed in Section S2, Supporting Information.

The evaluation of the zinc interstitial and oxygen atomic concentrations across the loaded graphene samples with ZnO nanocatalysts based on pristine and grafted GO surfaces was further investigated via XPS. This allowed the correlation of surface density to the concentration of suspended ZnO nanocatalysts during the loading process, as exhibited in Figure S8, Supporting Information. Spectra with a similar Zn content were observed for both series of the loaded samples based on pristine and grafted surfaces at 1021.8 ± 0.2 and 1044.9 ± 0.2 eV which can be assigned to Zn $2p_{3/2}$ and Zn-$2p_{1/2}$ core levels, respectively.[40] Those distinct singular spectra confirm the

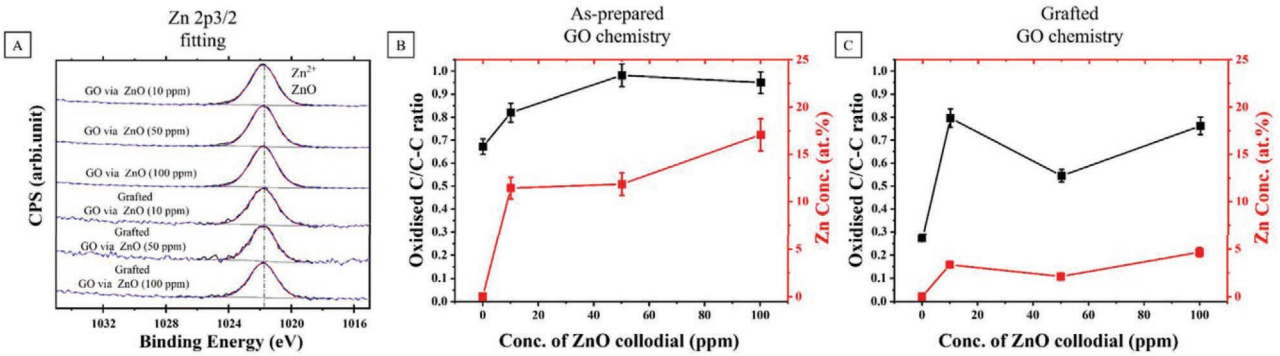

Figure 4. A–C) XPS analysis of zinc interstitial and oxygen atomic concentrations across loaded samples at different concentrations of nanocatalysts colloidal that include 10, 50, and 100 ppm during the loading process.

presence of ZnO species across the loaded samples post the loading process, as exhibited in **Figure 4**A. The pristine samples loaded with a 10-ppm colloid exhibited relative Zn content of 11.6 at%, while the samples loaded with 100 ppm showed 17.3 at% in agreement with previous reports.[32] In comparison to the other loaded samples based on pristine materials, the surface-modified samples showed relatively low Zn concentrations at the same range of loading conditions. For instance, the maximum Zn content was nearly 4 at% across this series for those loaded samples regardless of the loading conditions, suggesting a degree of selective behaviors for the grafted surfaces during the adsorption of those suspended nanocatalysts in different colloidal concentrations. Both series of loaded graphene samples also exhibited spectra at 532.0 ± 0.2 eV, which could be associated with oxygen doubly bound to the aromatic rings, for example, an epoxy structure,[41] based on the pristine and surface-modified chemistries.[42] Further, a second peak can be fitted at 530.2 ± 0.2 eV being assigned to either ZnO chemistry or compatible oxide with O^{2-}, as interpreted in Figure S9, Supporting Information.[43]

Analysis was carried out on the C1s spectra to quantify the variation of type and contribution of specific functional groups, which were developed across the pristine and grafted samples and then associated with the different loading conditions. Figure S10, Supporting Information, presents the high-resolution spectra of C1s for each series of pristine and grafted samples which broadly confirm the surface elemental compositions. Two major peaks observed at 284.2 and 286.3 eV (±0.2) corresponded to the C—C bond with sp^2 and graphite oxide, respectively. Interestingly, a third major C species was observed at 285.6 ± 0.2 eV, indicating the presence of partially oxidized graphite and this increased with the presence of ZnO nanocatalysts across the loaded samples based on as-prepared and grafted substrates. Other oxygen-related functional groups were detected at 288.1 and 289.2 eV (±0.2 eV) and were attributed to carbonyl (C=O) and carboxylic (COOH), respectively.[44,45] No significant changes in the carbonyl and carboxylic groups were seen across the postcatalysis loading process.

The impact of the nanocatalyst loading on the variation of the C oxide concentrations across the series of pristine and grafted GO samples was also evaluated by analyzing the oxidized C species versus C—C ratio obtained from XPS C fitting, respectively. Figure 4B,C exhibited an obvious increase of oxidized species of C including C—O and C=O, compared with C—C sp^2 across loaded samples, regardless of the surface chemistry conditions. The ratio of oxidized C to C—C increases with the increase of the concentration of colloidal used during the loading process as can be seen by the increase of the 285.6 ± 0.2 eV peak in Figure S10, Supporting Information. The outcome implies that upon the loading of ZnO colloidal, the GO as substrate can be further oxidized. By contrast, the overall oxidized C species weights were higher across the loaded samples based on the pristine GO compared to the surface-modified substrates. This may illustrate that the guided-etching methodology based on a particulate-nano template is likely to be initiated once the nanocatalysts anchor on the graphitic structure and then developed further based on the stimuli sources, for instance, the UV–visible irradiation in this study.

The mechanism of anchoring such ZnO nanocatalysts across pristine and grafted GO surfaces is likely to have occurred via physisorption interactions due to the difference of electrostatic charges between the suspended ZnO nanocatalyst, which are peripherally dominated with hydroxyl ligands[46] and can move freely in an ethanolic medium via Brownian motion. Also, the negatively charged surface of pristine and grafted GO, decorated with oxygenous functional groups across the graphitic surfaces and at their unsaturated edges,[27] may assist adsorption. Using these ZnO particle loading conditions, the surface density of nanocatalysts can be precisely tuned in the range of 1–10^3 particle/μm^2 across a 2D graphene structure and preserves their nucleated morphology. This refers to the installation of carboxyl moieties over graphene's graphitic planes to modify its surface. As a result, the grafted graphene substrates' chemical homogeneity may reduce the clustering of such nanocatalysts during the loading process. However, further theoretical studies are required to better understand the molecular interactions between nanocatalysts suspended in a colloidal solution and the installation of functional groups on graphene surfaces.

3.3. Pore Formation Kinetics Based on Photo-Irradiation

To give more insight into the pore formation process, the evolution of pore depth according to the penetration of the loaded

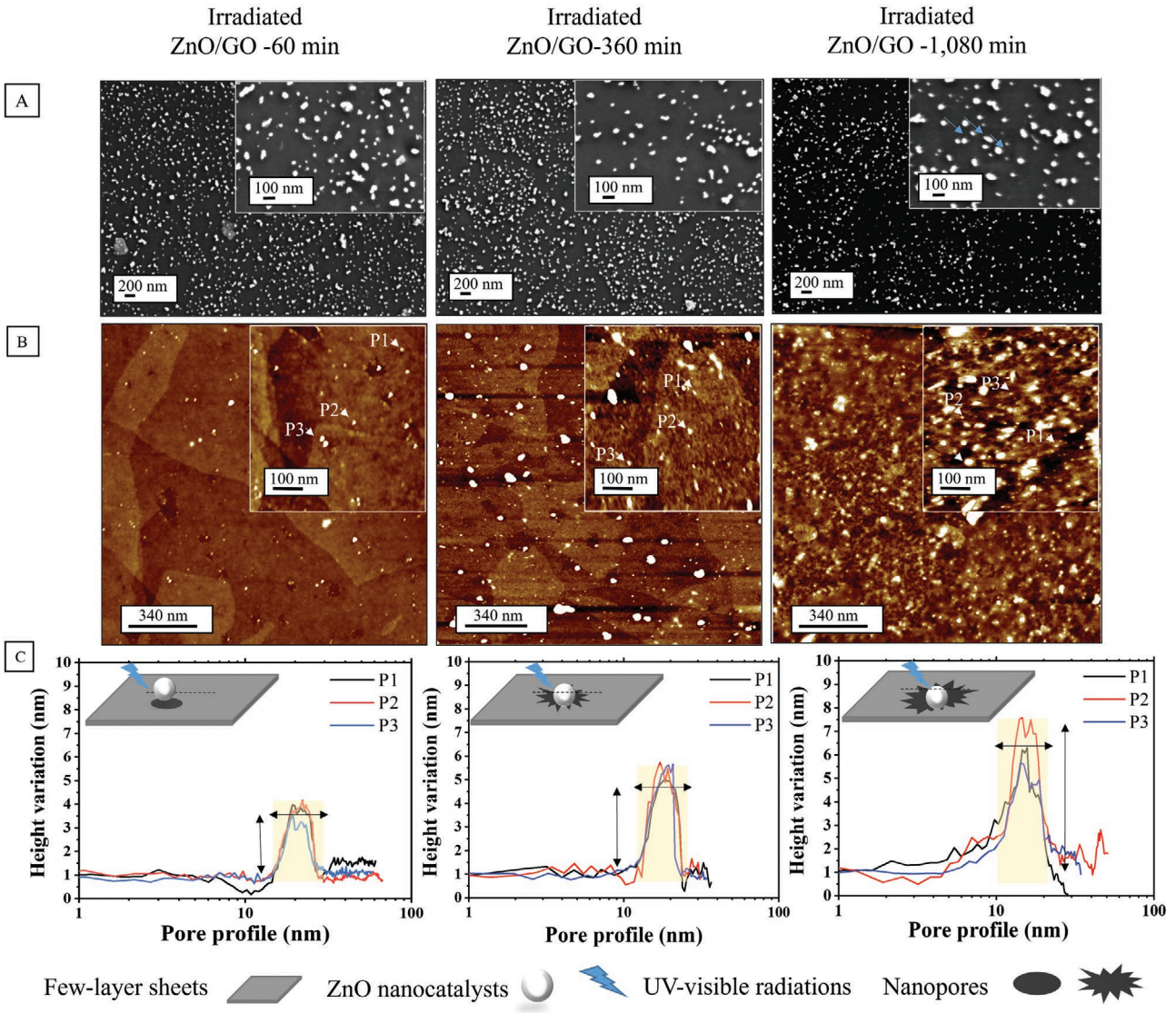

Figure 5. Morphological structures analysis of the loaded GO samples with ZnO nanocatalysts post the UV–visible irradiation process. A) FESEM micrographs and B) 2D-AFM maps for the irradiated samples that were loaded of nanocatalysts at fixed distribution 10^3 particle/μm^2. C) Representative profiles across the irradiated samples at different irradiation durations; inserts represent schematic diagrams illustrating the pore formation and expending based on the irradiation durations at different durations that include 60, 360, and 1080 min, separately. Color bars of the heights correspond to 20 and 10 nm of a resolution map at 340 and 100 nm scale bar, respectively.

nanocatalysts across few-layer graphene nano-assemblies with the irradiating duration was examined via SEM analysis. This was carried out via irradiating those samples loaded at a 100-ppm colloidal concentration of nanocatalysts at a fixed irradiance power density, typically of 1100 mW cm^{-2} for different durations that include 60, 360, and 1080 min, respectively. No significant morphological changes have been observed around those loaded nanocatalysts over graphitic structure after the irradiation for 60 and 360 min, whilst for those samples irradiated over 1080 min, a few ZnO nanocatalysts had penetrated the graphitic basal planes at the sub-nanometer level. However, samples irradiated for 1080 min exhibited graphitic basal planes intercalated with nanocatalysts, which had entirely penetrated through the graphitic nanostructure after irradiation, as highlighted by blue arrows in **Figure 5**A.

To evaluate the pore size and depth, as a result of nanocatalyst penetration, samples were also characterized via AFM mapping. Interestingly, samples irradiated for 60 min exhibited that nanocatalysts had penetrated their graphitic planes that were not revealed by SEM analysis. This suggests that sample irradiation for 60 min should be enough to perforate the graphene structure under this range of irradiation conditions. It is possible that these GO nano-assemblies have almost the same thickness (≤10 nm) and thus the smaller nanocatalysts with sizes on the same order of the thickness of a few-layer GO structure may penetrate completely into the graphitic structure, and become not visible (blue arrows). Conversely, other larger nanocatalysts (e.g., ≤30–50 nm) could be observed more apparently by either AFM or SEM after the irradiation process, as they protrude from the top of the GO assembly. Unpredictably, the representative

profiles around the nanocatalysts with an average size of ≤20 nm showed a slight increase in the height variation between the particle surface and the graphitic planes with the development of the irradiation duration across the irradiation samples. For instance, the samples irradiated for 1080 min showed an average height variation of ≤6 nm, while other samples etched for 360 and 60 min exhibited height variation values of ≤4 and ≤2 nm, respectively, as exhibited in Figure 5C. Evaluating the pore-depth across NPG assemblies however require more knowledge about the chemistry, besides the lateral resolution of AFM mapping, which can be provided via AFM-IR analysis.[47]

To attain 2D porous graphitic scaffolds the nanocatalysts must be removed, which is often performed via treatment with a mild (≈1 M, HCl) acid. In this regard, the time required to remove the nanocatalysts was systemically investigated. Loaded graphene assemblies which had been irradiated for 1080 min were treated with 1 M HCl in ambient conditions and analyzed separately at different durations (1, 6, 15, 72, and 168 h).

Examination of the microstructural morphology of these treated samples, via SEM and AFM analysis, showed that a significant portion of remaining nanocatalysts was bound to the pore boundary across the samples treated for 1.0 and 6.0 h. On the other hand, samples treated for 6.0 and 15.0 h, exhibited a minimal amount of the ZnO nanocatalysts, which had almost been removed from those treated samples for a long duration up to 168 h, as illustrated in Figure S11, Supporting Information. These results may highlight the chemical reactivity potential of dangling bonds to trap and localize such nanocatalysts at the pore boundary across the perforated graphene samples, compared with pristine materials.

To evaluate the impact of the acid treatment on the pore formation process and the chemical stability of the pristine materials during the nanocatalyst removal process, the variation of oxygenous functional groups across the graphene structure was evaluated via ATR-FTIR and Raman spectroscopy (Figure S12, Supporting Information). If the acid treatment has contributed to the pore formation, more edged carbon atoms across graphene sheets–in the form of oxygen-containing functional groups–are expected to be generated around pores. However, no further development of oxygen-containing groups across the graphene layer was observed post the acid treatment at different durations up to 168 h. The density of defects across GO nano-assemblies was also evaluated via Raman analysis (Figure S12C, Supporting Information). A slight increase in the I_D/I_G ratio was observed across the treatment over long duration periods up to 168 h, as illustrated in Figure S12D, Supporting Information. To clarify this increase seen in the density of defective sites, the morphology of such samples was investigated via AFM analysis. The acid treatment duration of 168 h for the pristine materials led to the activation of the graphitic planes with superficial nanopores (≤10 nm) and the doubling of the RMS roughness values compared to the as-produced graphene samples, as illustrated in Figure S13, Supporting Information. With these results, the acid treatment can extend the size of the intrinsic atomic defective sites in a range from a few angstroms to a couple of nanometers in the graphitic planes across GO nanostructure. This is in good agreement with the literature.[48,49] Further experiments, beyond the scope of the current study, for probing such atomic defective sites across graphene structure during the acid treatment, would provide a further understanding of the size expansion during the acid treatment at different conditions.

The size and density of pores formed, as well as depth profiles, were evaluated via AFM mapping, after ZnO digestion, and correlated to irradiation duration. Samples irradiated for 60 min possessed a size distribution of nanopores with 11 ± 12 nm, while other irradiated samples showed an increase in the pore size ranges, typically of 20 ± 15 and 40 ± 41 nm for 360 and 1080 min, respectively (**Figure 6**D). The impact of the irradiation duration on the pore depth profiles and geometry shapes was evaluated across those perforated samples that were irradiated at different durations. These were interpreted via selecting two size ranges of pores across the maps typical of 20 and 50 nm, as highlighted by the white arrows and circular profiles, respectively in Figure 6A. According to the line profiles across those pores with 20 nm size, the edges of pores tend to be much brighter across the maps of those perforated samples that were irradiated for 1080 min, as exhibited in the inserts in Figure 6B. The brighter regions observed around pore boundary have been reported in the previous studies and are attributed to the development of mechanical stress[14,50] at the edges of pores generated either through the intercalation or detaching of such nanocatalysts. These findings were found in agreement with the increase seen in the height variation between the nanocatalysts and graphitic planes prior to the removal of nanocatalysts, as illustrated in Figure 5C. This may indicate that the pore depth can be much deeper across the perforated samples that were irradiated for 1080 min, compared with other samples at short durations. For the relatively large pores ≤50 nm, the pore boundary was observed to be expanded with the increasing of the irradiation duration and to be more irregular post the removal of nanocatalysts during the acid treatment, as illustrated by the white circles in Figure 6A. Moreover, the samples that were irradiated for 360 and 1080 min exhibited an enlargement of the sizes of generated pores across their upper graphitic planes, which suggests that the conical-shaped nanochannels can be generated across such multilayer GO samples with the development of the irradiation duration during the perforation process. This procedure is therefore supposed to leave nanopores behind them with the maximum pore-depth across the graphitic structures.

3.4. Fine-Tuning of the Porosity Parameters across Perforated Graphene Based on Its Surface Chemistries

The porosity parameters of such 2D porous graphitic scaffolds in terms of sizes, densities, and depths across perforated graphene were investigated via AFM analysis based on pristine and grafted samples. This was typically then correlated to the loading conditions of such nanocatalysts prior to the irradiation process. **Figures 7**A and C represent AFM maps of the perforated samples that were previously prepared by different colloidal concentrations that include 10, 50, and 100 ppm during the loading process based on pristine and grafted chemistries, respectively.

The perforated samples previously loaded with 10 and 50 ppm ZnO nanoparticles exhibited size distribution values

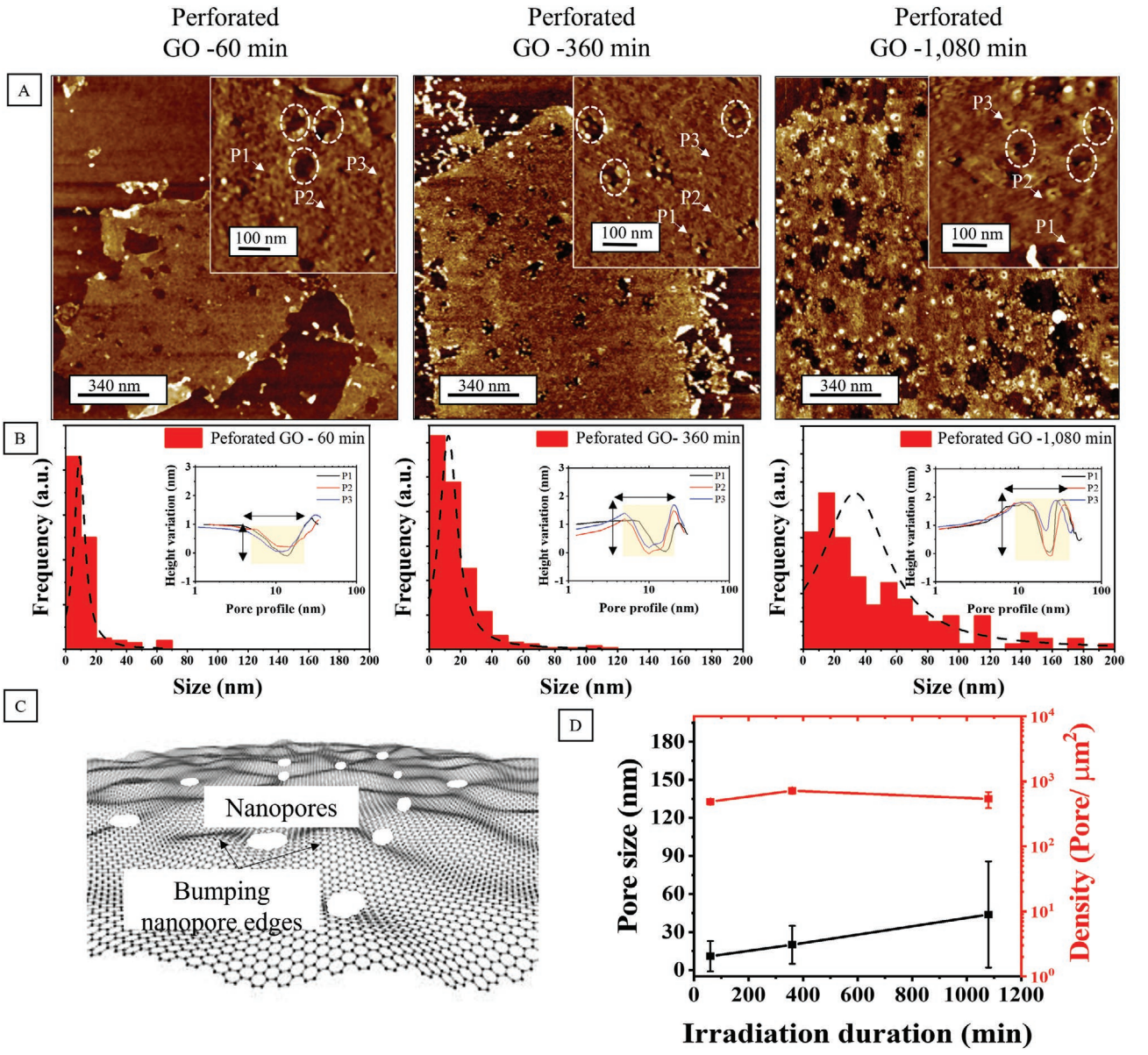

Figure 6. Morphological structures analysis of the perforated GO samples post the removal of nanocatalysts. A) 2D-AFM maps of perforated that were irradiated at different durations that include 60, 360, and 1080 min, separately at fixed distribution 10^3 particle/μm^2. B) The pore analysis in term of the size distributions and depth profiles for the perforated samples at different irradiation durations. C) Schematic diagram illustrating the pore formation process and the bumping occurs around the pore edges across the graphitic planes. D) The correlation of the porosity parameters in terms of the sizes as a function of the irradiation duration. Color bars of the heights correspond to 10 and 5 nm of a resolution map at 340 and 100 nm scale bar, respectively.

of 12 ± 10 and 20 ± 15 nm, while those perforated samples prepared with 100 ppm exhibited size distribution ranges of 40 ± 41 nm, respectively. This suggests that the generated pores can be merged, that is, nanocracks can be reduced across the pristine GO structure via tuning the concentration of used nanocatalysts. The density of generated pores across GO samples was found to follow the morphological properties of the designed particulate template and be able to be tuned via controlling the nanocatalyst concentration and then irradiated at fixed conditions (irradiance of 1100 mW cm^{-2} for 1080 min duration), as illustrated in Figure 7B. As an additional strategy, the incorporation of the phenylcarboxylate groups may serve as an anchoring mechanism for the ZnO nanocatalysts, allowing them to distribute evenly across the substrate surface.

The impact of incorporating the phenylcarboxylate layer after the loading of nanocatalysts and the irradiation process procedure was evaluated at different ZnO concentrations. Interestingly, when using the surface-modified graphene substrate, a significantly narrower distribution of pores (20 ± 12 nm) was observed when loaded in a 100 ppm ZnO colloid. This is equivalent to two times less than that obtained via the same protocol and relying on the innate graphene surface chemistry. Those

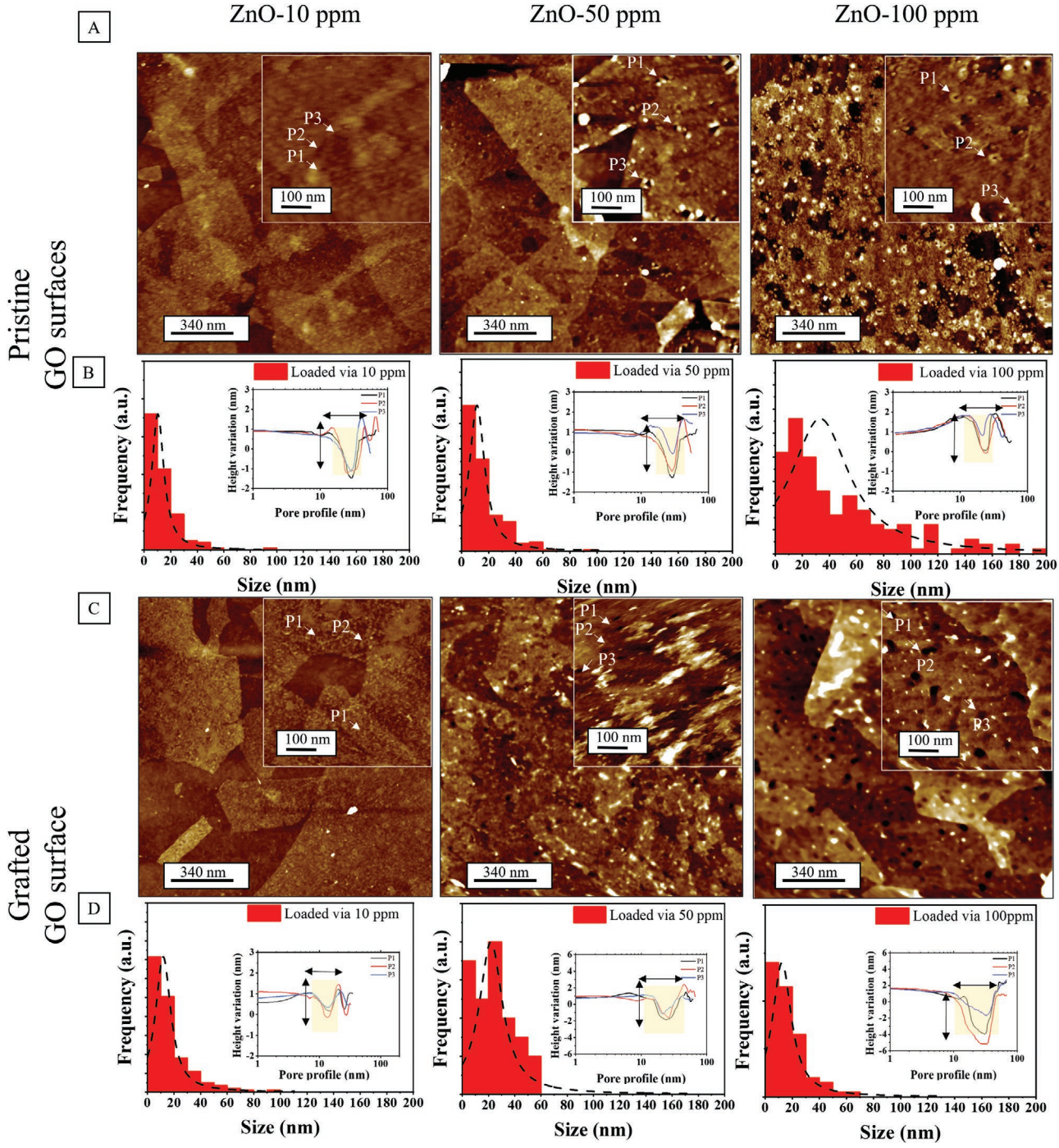

Figure 7. Morphological structure analysis of perforated nano-assemblies at different loading amounts of nanocatalysts. A,C) 2D-AFM maps of the perforated pristine and grafted GO nanostructure that were previously loaded at different concentrations that include 10, 50, and 100 ppm, separately, and then irradiated at a fixed duration (1080 min). B,D) The pore analysis in term of the size distributions and inserts illustrate the pore profiles across those perforated samples based on their surface chemistries. Color bars of the heights correspond to 10 and 5 nm of a resolution map at 340 and 100 nm scale bar, respectively.

samples using a surface modification approach demonstrated a pore density of 10^3 pore/μm^2, which is almost the same as that achieved by pristine materials. As an additional benefit, the surface modification has also overcome the merging issue between generated pores at the same perforation conditions, generating a much more homogeneous and controlled perforated structure. Moreover, the representative profiles of the modified substrates revealed more cylindrical-shaped pores, with a much deeper cavity compared with the conical geometry observed for the pristine material, as exhibited in Figure 7B,D.

3.5. Insight into the Photocatalytic Perforation Mechanism

The pore formation process was elucidated by Raman analysis, via monitoring the variation of crystallographic properties of the graphene structure, by comparing the 2D-to-G and D-to-G band ratio during photocatalytic perforation stages.[10,51–53] The results were summarized and tabulated in Table S3, Supporting Information. Raman spectra of pristine and grafted GO samples exhibited several peaks, corresponding to the D-, G-, D′-, G′-, and D+D′-band. G- and G′-bands during the photocatalytic perforation stages, as illustrated in spectra in Figure S14, Supporting Information.

The impact of the electrochemical grafting on the graphene lattices was assessed based on Raman spectra for grafted samples. The grafted GO samples showed I_D/I_G ratio values similar to those obtained by the pristine analogues prior to surface grafting. This suggests that the grafting process has minimal influence on the formation of atomic defective sites across GO lattices, in agreement with other findings in the literature.[54,55] To shed light on the impact of electrochemical grafting on the development of defective sites across the graphitic structure, the revealed trends were compared to other grafting studies using other graphene structures, typically CVD-grown graphene[36] and graphene nanoribbons[56] in their grafting experiments. Such graphene materials indeed exhibited an increase in the defect density post the electrochemical grafting, which is not in agreement with our findings. This inconsistency may be ascribed to the crystallographic properties of the raw graphene used during their electrochemical grafting experiments, as CVD-grown graphene and graphene nanoribbons were considered as unperturbed graphitic structures in comparison with these GO samples used in this study with their sp^3 hybridized bonds, thus the conjugated sp^2-network is already perturbed prior to the electrochemical grafting.[36] Considering that the surface modification process is carried out using cyclic voltammetry (–1 to +1 V, vs Ag/AgCl), the reductive electrochemical potential may have increased the crystallinity of graphene lattice.[57] No change of I_{2D}/I_G ratio was however observed after electrochemical grafting, indicating lower amounts of sp^3-hybridization defects created on graphitic planes and minor changes in their crystallographic during the grafting process in this range of conditions.

As grafted GO samples were vertically dipped into nanocatalyst colloidal at 100 ppm concentration, the I_D/I_G ratio increased by nearly 10% compared to their grafted samples prior to the loading process, which is in good agreement with other perforation studies.[32,52] This increase in the defect density may be attributed to the physisorption of nanocatalysts on grafted graphitic planes, which are expected to develop a higher amount of sp^3-hybridization defects across graphene samples. The I_{2D}/I_G ratio increased from 0.080 to 0.342 after the loading process, as a result of remarkable increase in the crystallinity nature of such grafted samples. The development of crystallinity properties may be ascribed to the nanoparticle adsorption across graphitic planes, which is likely to occur through the interaction of the hydroxyl groups on the nanocatalyst surface with the carboxyl groups within defect sites on the GO sheets.[27] Such interactions may lead to minimizing the concentration of functional groups, which is suggesting a partial restoring of the sp^2-conjugated network.[58,59] Interestingly, the grafted GO samples showed an I_{2D}/I_G ratio less than that of pristine materials, which may refer to a preferential adsorption reaction of nanocatalysts with grafted GO surfaces during the loading process. These findings were found in a good match with the low zinc interstitial across those loaded samples based on the surface-modified chemistry compared with the pristine structure, which had been revealed via XPS analysis.

After UV–visible irradiation in an aqueous medium for 1080 min, a significant decrease in the magnitude of I_{2D}/I_G ratios was observed. This indicates that the irradiation process in the presence of nanocatalysts may reduce the crystalline nature of graphene nanostructure, as would be expected with the formation of nanopores, as shown in **Figure 8**A,B. Such activated pores are also expected to leave graphitic planes decorated with more oxygenous functional groups after the photo-etching process, typically carboxylic and carbonyl groups around the edges of generated pores. Thus, a further increase in the sp^3-hybridization defects across the perforated graphene structure is typically observed.[60–62] The NPG samples based on the modified surface with the aryl-diazonium salt, exhibited no change in the I_D/I_G similar to other perforated samples based on pristine GO nanostructure after nanocatalyst removal. Those perforated graphene samples demonstrated an increase in the crystallinity nature across their graphitic structure that suggests a degree of chemical reduction of the previously produced functional groups during the photo-etching process.[63,64]

To highlight the role of installed surface chemistry of graphene and the nanocatalyst functionality during perforation, control experiments were conducted using other graphene materials, for example, RGO, with minimal oxygenous functional groups. RGO samples (control) showed no significant change in the density of defects and demonstrated a constant I_D/I_G ratio during the photocatalytic perforation stages as shown in Figure 8A. This may be attributed to the high defective nature of RGO structures, with an I_D/I_G ratio of nearly 1.4. An increase in RGO crystallinity was observed after the loading of nanocatalysts to the RGO surfaces, though this increase was smaller, relative to loaded pristine and grafted GO samples (check blue circle in Figure 8B). This suggests minimal interaction between graphitic planes and nanocatalysts, as the chemical reduction via exposure to N_2H_2 vapor tends to leave the graphitic planes with a lower concentration of functional groups that can be reduced later via the phototreatment.[27,65] Interestingly, the irradiated RGO samples exhibited a similar trend of the crystallinity nature to that of irradiated pristine, and grafted GO samples. However, no nanopores were observed across treated RGO samples, as illustrated in Figure S15, Supporting Information.

In order to emphasize the role of UV radiation on the development of defects across the graphene materials at different irradiation conditions in terms of powers and durations, the microstructure morphology analysis of irradiated GO films was considered.[66] The GO films irradiated at 305–315 nm exhibited a sharp decrease in the oxygen-related functionalities. Other films, irradiated at a wavelength range of 310–380 nm for up to 480 min, led only to atomic defective sites, as well as the amorphization across the graphitic structure, with no nanopores being observed. With these findings, the role of nanocatalysts and the grafting layer in localizing the pore formation

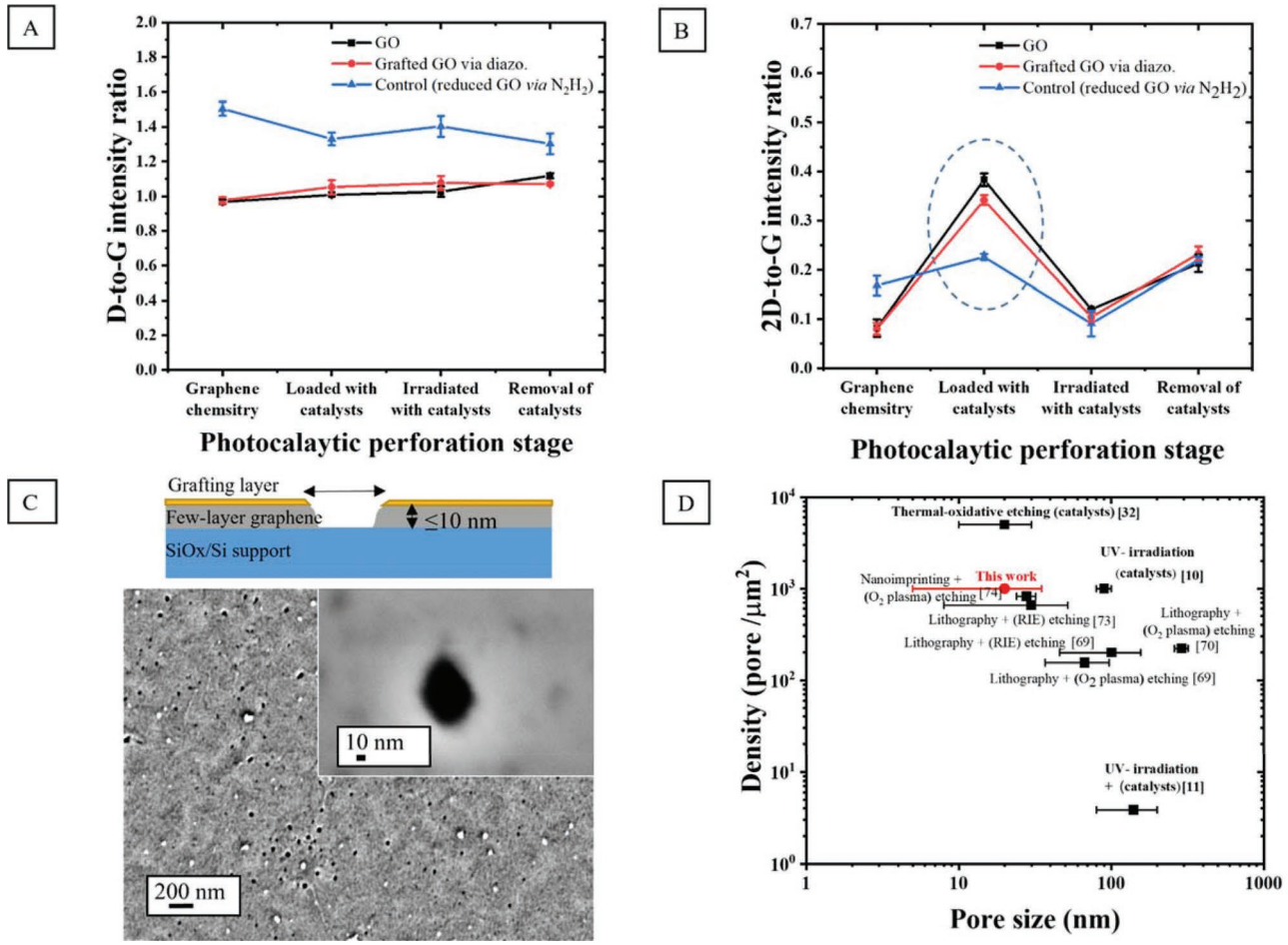

Figure 8. A,B) Raman analysis of crystallographic properties for surface graphene chemistries during photocatalytic perforation stages in terms of (A) defect density and (B) crystallinity nature. C) Schematic diagram illustrating the mechanism of the pore formation based on the proposed photocatalytic perforation and FESEM micrographs of perforated graphene-based on diazonium chemistry of 10^3 pore/μm^2 at a resolution of 200 nm and 10 nm, respectively. D) The benchmarking of the photocatalytic methodology in light of the state of the art of perforation methodologies.[10,11,32,69,70,73–75]

during the photo-excitation mechanism,[10,11] as well as the UV irradiation duration to ablate few carbon clusters from the graphitic structure during the photocatalytic perforation protocol, is demonstrated and illustrated in Figure 8C. Based on the photo-etching process, ZnO nanocatalysts as pore-mediators may lower the activation energy necessary to induce site-selective pores across graphene.[14] This may have occurred through stimulating free radicals during photo-excitation. However, in situ perforation experiments[11,67,68] for probing such short-lived oxygen-derived radicals created during the reaction will provide a better understanding of the perforation mechanism. The heating effect of UV irradiation, on the other hand, cannot be neglected, especially when loaded samples are irradiated for long periods. While this heating may play a role in the etching process, we consider that by initiating oxidative etching, the UV light is the primary source of pore formation.

To benchmark the perforation performance of the proposed protocol, the achieved porosity parameters by this photocatalytic perforation methodology have been compared with those obtained by other guided-etching perforation methodologies including nanolithography[69,70] and particulate-template[12,71] techniques. Those techniques offer distinct ranges of pore size distributions in a range of 20–200 nm, as well as pore densities from 10^1 to 10^3 pores/μm^2, as summarized and tabulated in Table S3, Supporting Information. The achieved porosity parameters in this work were found to be on the same order of performance as other lithographic techniques. Here, the achieved porosity parameters of such perforated graphene nano-assemblies in terms of sizes, densities, and depths were engineered by controlling the proposed photocatalytic perforation conditions. This perforation protocol not only overcomes the need for the external template but also offers a sustainable/environmental approach, avoiding using either highly corrosive chemicals, or high-temperature furnaces to incorporate pores across multilayer graphene assemblies. However, sculpting pores at the same dimension across 2D nano-assemblies using this approach may be problematic due to the difficulties of managing the morphological properties of such particles transferred to graphene surface at a sub-nanometer level.[4] To realize NPG membranes via the proposed protocol, the assembly of such sheets over the porous supports, followed by the perforation process is the optimal approach.[9,72] Utilizing the synergistic relationship between the pore-mediator morphology and

the graphene membrane thickness during the photo-etching process is a prerequisite to achieving membranes for practical uses.

4. Conclusions and Prospects

In the present work, we successfully perforated few-layer graphene assemblies using an aryl-diazonium chemistry-assisted nanocatalysts array. The sizes and densities of the nanocatalysts were controlled across particulate-nanotemplate during the nucleation and loading processes. Nanopores were engineered across graphene nanostructures with various pore size ranges of 20–100 nm depending on the irradiation duration. The perforation density was also tunable (10^1–10^3 pores/μm^2) on the same order of the loaded nanocatalysts to the graphene surfaces.

The uniformity of oxygen-related functional groups across graphene, via incorporating a surface modification layer, led to significantly narrower pore distribution, avoiding the merging of generated pores, that is, nanocracks across perforated nano-assemblies. The perforation mechanism was shown to be facilitated by semiconducting nanoparticles, for example, ZnO-NPs in this study, accelerating the oxidation of carbon clusters across the graphitic planes in direct contact with such nanocatalysts under UV–visible irradiation. The photocatalytic perforation methodology presented showed a practical route to fabricate perforated nano-assemblies based on 2D graphene over a centimeter-scale with the tunable porosity parameters (size, density, and depth) as that reported for lithographic techniques. This approach also avoids the complexity related to the nanolithographic perforation processes. Last, advanced geometries of the nanocatalysts in the photocatalytic perforation methodology can control the geometry of nanochannels, moving from conventional cylindrical-shape to more complex geometries to match the 3D structure of biomolecules, providing better performance for complex DNA sequencing and fractionation, to give more insight into the human genome functionality.

Supporting Information

Supporting Information is available from the Wiley Online Library or from the author.

Acknowledgements

A.G. thanks Deakin University for providing financial support through Deakin University Postgraduate Research Scholarship (DUPR). L.K. acknowledges his Ambassador Technology Fellowship at the Melbourne Centre for Nanofabrication (MCN), the Victorian Node of the Australian National Fabrication Facility (ANFF), where the AFM mappings were performed. Deakin University's Advanced Characterization Facility is acknowledged for use of the Electron Microscopy Facility and Dr. Andrew Sullivan is acknowledged for his advice and guidance during imaging. L.F.D. acknowledges the Australian Research Council for his Discovery Early Career Researcher Award (DECRA – DE180100130). The authors would like to acknowledge the support of the ANFF and Australian Microscopy & Microanalysis Research Facility (AMMRF) regarding using experimental equipment. The authors acknowledge Flinders Microscopy and Microanalysis and the expertise.

Open access publishing facilitated by Deakin University, as part of the Wiley - Deakin University agreement via the Council of Australian University Librarians.

Conflict of Interest

The authors declare no conflict of interest.

Data Availability Statement

The data that support the findings of this study are available from the corresponding author upon reasonable request.

Keywords

nanoperforation, nanoporous graphene, porosity analysis

Received: October 31, 2021
Revised: December 13, 2021
Published online: January 31, 2022

[1] M. S. Boutilier, D. Jang, J.-C. Idrobo, P. R. Kidambi, N. G. Hadjiconstantinou, R. Karnik, *ACS Nano* **2017**, *11*, 5726.
[2] S. Huang, M. Dakhchoune, W. Luo, E. Oveisi, G. He, M. Rezaei, J. Zhao, D. T. L. Alexander, A. Züttel, M. S. Strano, K. V. Agrawal, *Nat. Commun.* **2018**, *9*, 2632.
[3] L. F. Dumée, C. Feng, L. He, Z. Yi, F. She, Z. Peng, W. Gao, C. Banos, J. B. Davies, C. Huynh, *Carbon* **2014**, *70*, 313.
[4] A. Guirguis, J. W. Maina, L. Kong, L. C. Henderson, A. Rana, L. H. Li, M. Majumder, L. F. Dumée, *Carbon* **2019**, *155*, 660.
[5] W. Yuan, J. Chen, G. Shi, *Mater. Today* **2014**, *17*, 77.
[6] Y. Lin, Y. Liao, Z. Chen, J. W. Connell, *Mater. Res. Lett.* **2017**, *5*, 209.
[7] S. Howorka, *Nat. Nanotechnol.* **2017**, *12*, 619.
[8] X. Qian, K. Xie, S. Guo, Q. Liang, S. Zhang, Z. Xiong, H. Zhan, C. Liu, X. Yang, J. Zhu, D. Li, *Chem. Commun.* **2020**, *56*, 7005.
[9] A. Guirguis, J. W. Maina, X. Zhang, L. C. Henderson, L. Kong, H. Shon, L. F. Dumée, *Mater. Horiz.* **2020**, *7*, 1218.
[10] O. Akhavan, *ACS Nano* **2010**, *4*, 4174.
[11] J. G. Radich, P. V. Kamat, *ACS Nano* **2013**, *7*, 5546.
[12] D.-P. Yang, X. Wang, X. Guo, X. Zhi, K. Wang, C. Li, G. Huang, G. Shen, Y. Mei, D. Cui, *J. Phys. Chem. C* **2013**, *118*, 725.
[13] S. P. Koenig, L. Wang, J. Pellegrino, J. S. Bunch, *Nat. Nanotechnol.* **2012**, *7*, 728.
[14] S.-S. Kim, M. J. Park, J.-H. Kim, G. Ahn, S. Ryu, B. H. Hong, B.-H. Sohn, *Chem. Mater.* **2015**, *27*, 7003.
[15] H. Yamaguchi, G. Eda, C. Mattevi, H. Kim, M. Chhowalla, *ACS Nano* **2010**, *4*, 524.
[16] D. Li, M. B. Müller, S. Gilje, R. B. Kaner, G. G. Wallace, *Nat. Nanotechnol.* **2008**, *3*, 101.
[17] P. Sharma, M. R. Das, *J. Chem. Eng. Data* **2013**, *58*, 151.
[18] S. Thangavel, G. Venugopal, *Powder Technol.* **2014**, *257*, 141.
[19] M. H. Gharahcheshmeh, C. T.-C. Wan, Y. A. Gandomi, K. V. Greco, A. Forner-Cuenca, Y.-M. Chiang, F. R. Brushett, K. K. Gleason, *Adv. Mater. Interfaces* **2020**, *7*, 2000855.
[20] M. Hilder, B. Winther-Jensen, D. Li, M. Forsyth, D. R. MacFarlane, *Phys. Chem. Chem. Phys.* **2011**, *13*, 9187.
[21] C. L. Arnold, D. J. Eyckens, L. Servinis, M. D. Nave, H. Yin, R. K. Marceau, J. Pinson, B. Demir, T. R. Walsh, L. C. Henderson, *J. Mater. Chem. A* **2019**, *7*, 13483.

[22] D. J. Eyckens, C. L. Arnold, J. D. Randall, F. Stojcevski, A. Hendlmeier, M. K. Stanfield, J. Pinson, T. R. Gengenbach, R. Alexander, L. C. Soulsby, *ACS Appl. Mater. Interfaces* **2019**, *11*, 41617.
[23] D. J. Eyckens, B. Demir, J. D. Randall, T. R. Gengenbach, L. Servinis, T. R. Walsh, L. C. Henderson, *Compos. Sci. Technol.* **2020**, *196*, 108225.
[24] D. J. Eyckens, J. D. Randall, F. Stojcevski, E. Sarlin, S. Palola, M. Kakkonen, C. Scheffler, L. C. Henderson, *Composites, Part A* **2020**, *138*, 106053.
[25] D. J. Eyckens, F. Stojcevski, A. Hendlmeier, C. L. Arnold, J. D. Randall, M. D. Perus, L. Servinis, T. R. Gengenbach, B. Demir, T. R. Walsh, L. C. Henderson, *Chem. Eng. J.* **2018**, *353*, 373.
[26] E. Bekyarova, M. E. Itkis, P. Ramesh, C. Berger, M. Sprinkle, W. A. de Heer, R. C. Haddon, *J. Am. Chem. Soc.* **2009**, *131*, 1336.
[27] S. Pei, H.-M. Cheng, *Carbon* **2012**, *50*, 3210.
[28] M. Y. Ge, H. P. Wu, L. Niu, J. F. Liu, S. Y. Chen, P. Y. Shen, Y. W. Zeng, Y. W. Wang, G. Q. Zhang, J. Z. Jiang, *J. Cryst. Growth* **2007**, *305*, 162.
[29] A. Guirguis, S. R. Polaki, G. Sahoo, S. Ghosh, M. Kamruddin, A. Merenda, X. Chen, J. W. Maina, G. Szekely, L. Dumee, *Carbon* **2020**, *168*, 32.
[30] A. Merenda, A. Rana, A. Guirguis, D. M. Zhu, L. Kong, L. F. Dumée, *J. Phys. Chem. C* **2019**, *123*, 2189.
[31] S. Huh, J. Park, Y. S. Kim, K. S. Kim, B. H. Hong, J.-M. Nam, *ACS Nano* **2011**, *5*, 9799.
[32] H.-K. Kim, S.-M. Bak, S. W. Lee, M.-S. Kim, B. Park, S. C. Lee, Y. J. Choi, S. C. Jun, J. T. Han, K.-W. Nam, *Energy Environ. Sci.* **2016**, *9*, 1270.
[33] S.-S. Li, Y.-K. Su, *RSC Adv.* **2019**, *9*, 2941.
[34] A. V. Ellis, A. Al-deen, H. Dalal, G. G. Andersson, *J. Phys. Chem. C* **2013**, *117*, 21312.
[35] S. Phal, B. Shatri, A. Berisha, P. Geladi, B. Lindholm-Sethson, S. Tesfalidet, *J. Electroanal. Chem.* **2018**, *812*, 235.
[36] Z. Xia, F. Leonardi, M. Gobbi, Y. Liu, V. Bellani, A. Liscio, A. Kovtun, R. Li, X. Feng, E. Orgiu, P. Samorì, E. Treossi, V. Palermo, *ACS Nano* **2016**, *10*, 7125.
[37] J. Greenwood, T. H. Phan, Y. Fujita, Z. Li, O. Ivasenko, W. Vanderlinden, H. Van Gorp, W. Frederickx, G. Lu, K. Tahara, Y. Tobe, H. Uji-i, S. F. L. Mertens, S. De Feyter, *ACS Nano* **2015**, *9*, 5520.
[38] J. Rafiee, X. Mi, H. Gullapalli, A. V. Thomas, F. Yavari, Y. Shi, P. M. Ajayan, N. A. Koratkar, *Nat. Mater.* **2012**, *11*, 217.
[39] Y. J. Shin, Y. Wang, H. Huang, G. Kalon, A. T. S. Wee, Z. Shen, C. S. Bhatia, H. Yang, *Langmuir* **2010**, *26*, 3798.
[40] S. U. Awan, S. K. Hasanain, J. Rashid, S. Hussain, S. A. Shah, M. Z. Hussain, M. Rafique, M. Aftab, R. Khan, *Mater. Chem. Phys.* **2018**, *211*, 510.
[41] R. Larciprete, S. Fabris, T. Sun, P. Lacovig, A. Baraldi, S. Lizzit, *J. Am. Chem. Soc.* **2011**, *133*, 17315.
[42] N. Mas, J. L. Hueso, G. Martinez, A. Madrid, R. Mallada, M. C. Ortega-Liebana, C. Bueno-Alejo, J. Santamaria, *Carbon* **2020**, *156*, 453.
[43] R. Al-Gaashani, S. Radiman, A. R. Daud, N. Tabet, Y. Al-Douri, *Ceram. Int.* **2013**, *39*, 2283.
[44] A. Ganguly, S. Sharma, P. Papakonstantinou, J. Hamilton, *J. Phys. Chem. C* **2011**, *115*, 17009.
[45] Z. Yi, A. Merenda, L. Kong, A. Radenovic, M. Majumder, L. F. Dumée, *Sci. Rep.* **2018**, *8*, 8154.
[46] S.-W. Bian, I. A. Mudunkotuwa, T. Rupasinghe, V. H. Grassian, *Langmuir* **2011**, *27*, 6059.
[47] S. Morsch, S. Lyon, S. Edmondson, S. Gibbon, *Anal. Chem.* **2020**, *92*, 8117.
[48] S. C. O'Hern, D. Jang, S. Bose, J.-C. Idrobo, Y. Song, T. Laoui, J. Kong, R. Karnik, *Nano Lett.* **2015**, *15*, 3254.
[49] M. H. Khan, M. Moradi, M. Dakhchoune, M. Rezaei, S. Huang, J. Zhao, K. V. Agrawal, *Carbon* **2019**, *153*, 458.
[50] Y. Liu, X. Chen, *J. Appl. Phys.* **2014**, *115*, 034303.
[51] O. Akhavan, E. Ghaderi, *Small* **2013**, *9*, 3593.
[52] D. Zhou, Y. Cui, P.-W. Xiao, M.-Y. Jiang, B.-H. Han, *Nat. Commun.* **2014**, *5*, 4716.
[53] M. A. Al Faruque, R. Remadevi, A. Guirguis, A. Kiziltas, D. Mielewski, M. Naebe, *Sci. Rep.* **2021**, *11*, 12068.
[54] J. R. Lomeda, C. D. Doyle, D. V. Kosynkin, W.-F. Hwang, J. M. Tour, *J. Am. Chem. Soc.* **2008**, *130*, 16201.
[55] Z. Jin, J. R. Lomeda, B. K. Price, W. Lu, Y. Zhu, J. M. Tour, *Chem. Mater.* **2009**, *21*, 3045.
[56] A. Sinitskii, A. Dimiev, D. A. Corley, A. A. Fursina, D. V. Kosynkin, J. M. Tour, *ACS Nano* **2010**, *4*, 1949.
[57] S. Rahpeima, E. M. Dief, S. Ciampi, C. L. Raston, N. Darwish, *ACS Appl. Mater. Interfaces* **2021**, *13*, 38799.
[58] G. Williams, B. Seger, P. V. Kamat, *ACS Nano* **2008**, *2*, 1487.
[59] P. V. Kamat, *Chem. Rev.* **1993**, *93*, 267.
[60] F. Niu, J.-M. Liu, L.-M. Tao, W. Wang, W.-G. Song, *J. Mater. Chem. A* **2013**, *1*, 6130.
[61] F. Schedin, A. Geim, S. Morozov, E. Hill, P. Blake, M. Katsnelson, K. Novoselov, *Nat. Mater.* **2007**, *6*, 652.
[62] M. A. Akhukov, A. Fasolino, Y. N. Gornostyrev, M. I. Katsnelson, *Phys. Rev. B* **2012**, *85*, 115407.
[63] A. K. Das, M. Srivastav, R. K. Layek, M. E. Uddin, D. Jung, N. H. Kim, J. H. Lee, *J. Mater. Chem. A* **2014**, *2*, 1332.
[64] S. Rao, J. Upadhyay, K. Polychronopoulou, R. Umer, R. Das, *J. Compos. Sci.* **2018**, *2*, 25.
[65] X. Gao, J. Jang, S. Nagase, *J. Phys. Chem. C* **2010**, *114*, 832.
[66] M. S. Mirshekarloo, M. Shaibani, M. C. D. Cooray, C. D. Easton, L. Bourgeois, S. Hernandez, P. Jovanović, L. F. Dumée, P. C. Banerjee, M. Majumder, *ACS Sustainable Chem. Eng.* **2020**, *8*, 1031.
[67] H. Fu, L. Zhang, S. Zhang, Y. Zhu, J. Zhao, *J. Phys. Chem. B* **2006**, *110*, 3061.
[68] P. Kumari, N. Bahadur, L. A. O'Dell, L. Kong, A. Sadek, A. Merenda, L. F. Dumée, *Sep. Purif. Technol.* **2021**, *258*, 118011.
[69] A. Sinitskii, J. M. Tour, *J. Am. Chem. Soc.* **2010**, *132*, 14730.
[70] N. S. Safron, A. S. Brewer, M. S. Arnold, *Small* **2011**, *7*, 492.
[71] J. Zhang, H. Song, D. Zeng, H. Wang, Z. Qin, K. Xu, A. Pang, C. Xie, *Sci. Rep.* **2016**, *6*, 32310.
[72] A. O. Rashed, A. Merenda, T. Kondo, M. Lima, J. Razal, L. Kong, C. Huynh, L. F. Dumée, *Sep. Purif. Technol.* **2021**, *257*, 117929.
[73] J. Bai, X. Zhong, S. Jiang, Y. Huang, X. Duan, *Nat. Nanotechnol.* **2010**, *5*, 190.
[74] X. Liang, Y.-S. Jung, S. Wu, A. Ismach, D. L. Olynick, S. Cabrini, J. Bokor, *Nano Lett.* **2010**, *10*, 2454.
[75] Z. Zeng, X. Huang, Z. Yin, H. Li, Y. Chen, H. Li, Q. Zhang, J. Ma, F. Boey, H. Zhang, *Adv. Mater.* **2012**, *24*, 4138.